Phonon anomalies within the polar charge density wave phase of the structurally chiral superconductor Mo_3Al_2C

Shangfei Wu [1,2,*] Xianghan Xu [1,3,4] Fei-Ting Huang [1,3] Turan Birol [5]
Sang-Wook Cheong [1,3] and Girsh Blumberg [1,6,†]

[1]*Department of Physics and Astronomy, Rutgers University, Piscataway, New Jersey 08854, USA*
[2]*Beijing Academy of Quantum Information Sciences, Beijing 100193, China*
[3]*Keck Center for Quantum Magnetism, Rutgers University, Piscataway, New Jersey 08854, USA*
[4]*School of Physics and Astronomy, University of Minnesota, Minneapolis, Minnesota 55455, USA*
[5]*Department of Chemical Engineering and Materials Science, University of Minnesota, Minnesota 55455, USA*
[6]*National Institute of Chemical Physics and Biophysics, 12618 Tallinn, Estonia*

(Received 25 February 2025; revised 28 April 2025; accepted 27 May 2025; published 10 June 2025)

We employ polarization-resolved Raman spectroscopy to study the lattice dynamics of the polar charge density wave phase of the superconductor Mo_3Al_2C with structural chirality. We show the phononic signatures of the charge density wave transition at $T^* = 155$ K in Mo_3Al_2C. The detailed temperature dependence of these phonon modes' frequency, half width at half maximum, and integrated area below T^* reveal anomalies at an intermediate temperature $T' \sim 100$ K, especially for the low-energy modes at 130 and 180 cm^{-1}. We discuss the origin of these phonon anomalies within the polar charge density wave phase of Mo_3Al_2C.

DOI: 10.1103/nkx2-6qyr

I. INTRODUCTION

In 1965, Anderson and Blount first proposed the concept of ferroelectric metals or polar metals [1]. Although they were proposed long ago and many compounds were predicted [2,3], only a few examples have been experimentally verified, as ferroelectricity and metallicity have traditionally been considered to be incompatible [4–6]. Hence, considerable attention is being directed towards exploring various unconventional mechanisms to realize polar metal phases [2,4–6]. The decoupled electron mechanism [1,7,8], which involves a significant separation between the density of states of polar modes and the Fermi level, results in the polar distortion being decoupled from the itinerant electrons surrounding the Fermi sea [9–12]. Another unconventional mechanism for the coexistence of polarization and conductivity was demonstrated experimentally by the switchable ferroelectric metal WTe_2 and $1T'$-$MoTe_2$ [13,14] via the interlayer sliding mechanism, which corresponds to the decoupled space mechanism. A third unconventional mechanism is polar bulking in hyperferroelectric metals resistant to itinerant electrons, as predicted in hexagonal *ABC* compounds (LiGaGe type) [15].

In principle, breaking symmetry through charge disproportionation and ordering can lead to the emergence of ferroelectricity. In other words, when a noncentrosymmetric charge modulation occurs, it can result in a potential net electric polarization [16–18]. This concept was proposed and studied in several *insulating* systems, such as magnetite Fe_3O_4 [19], bond-centered and site-centered $Pr_xCa_{1-x}MnO_3$ [20], mixed-valence compounds [21–23], and superlattice systems [24–27]. However, the phenomenon of charge ordering or charge density wave (CDW) driven polarization in *metallic* systems has been little studied.

Recently, Mo_3Al_2C was reported to be a CDW-driven polar metal coexisting with superconductivity and structural chirality [28]. Mo_3Al_2C has a cubic structure with space group $P4_132$ or $P4_332$ (point group O) at room temperature [Fig. 1(a)]. The crystal structure lacks inversion and mirror symmetries. It is noncentrosymmetric, chiral, and nonpolar at room temperature. Upon cooling down the sample, the measured resistivity shows a superconducting transition at $T_c = 8$ K and a dip at around $T^* = 155$ K [Fig. 1(b)] [29]. The anomalies at T^* were also reported in previous magnetic susceptibility, specific heat, and nuclear-magnetic-resonance measurements [29–32]. Our recent transmission electron microscopy and Raman scattering results established a CDW order below T^* in Mo_3Al_2C [28]. We also showed that the transition at T^* is a cubic-nonpolar to rhombohedral-polar transition driven by condensation of M_5 soft modes at three symmetry-equivalent wave vectors located at the Brillouin zone boundaries, creating a polarization along the threefold axis in the body-diagonal direction below T^* [28].

In this work, we present a detailed analysis of the lattice dynamics in the polar CDW phase of the superconductor Mo_3Al_2C using polarization-resolved Raman spectroscopy. We identify the phononic signatures associated with the CDW transition at $T^* = 155$ K in Mo_3Al_2C. An examination of the temperature dependence of the phonon modes' frequency, half width at half maximum, and integrated area below T^*, particularly for the modes at 130 and 180 cm^{-1}, reveals anomalies at an intermediate temperature, $T' \sim 100$ K. We propose that the lattice anomalies at T' within the CDW phase are possibly

*Contact author: wusf@baqis.ac.cn
†Contact author: girsh@physics.rutgers.edu

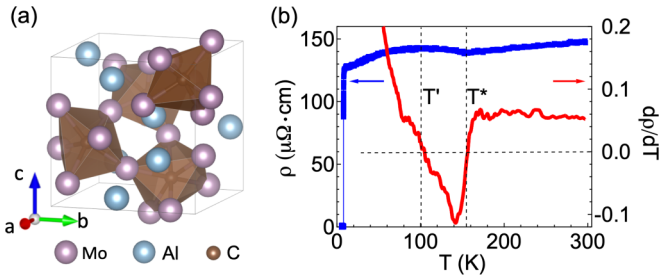

FIG. 1. (a) Crystal structure of Mo_3Al_2C (space group: $P4_132$ or $P4_332$). (b) Resistivity ρ of Mo_3Al_2C on the (0 0 1) surface recorded in a cooling-down process for the left axis. The right axis shows the first derivative of the resistivity as a function of temperature ($d\rho/dT$). The two vertical dashed lines denote the two anomaly temperatures, $T^* = 155$ K and $T' \sim 100$ K, corresponding to $d\rho/dT = 0$.

related to a change in the Mo displacements while the crystal symmetry remains unchanged.

II. EXPERIMENT AND METHODS

Single-crystal preparation and characterization. Single crystals of Mo_3Al_2C were grown using a slow cooling method described in Ref. [28]. Electric transport measurements were carried out using a standard four-point probe method in the (0 0 1) plane in a He exchanges gas environment using a physical property measurement system in a cooling-down process.

Raman scattering measurements. The polished Mo_3Al_2C crystals with a (0 0 1) plane and (1 1 1) plane used for the Raman scattering study were positioned in a continuous helium flow optical cryostat [33]. The Raman measurements were mainly performed using the Kr^+ laser line at 647.1 nm (1.92 eV) in a quasibackscattering geometry along the crystallographic c axis. The excitation laser beam was focused onto a 50×100 μm^2 spot on the ab plane, with the incident power around 12 mW. The scattered light was collected and analyzed by a triple-stage Raman spectrometer and recorded using a liquid-nitrogen-cooled charge-coupled device. Linear and circular polarizations are used in this study to decompose the Raman data into different irreducible representations. The instrumental resolution was kept better than 1.5 cm^{-1}. All linewidth data presented in this paper were corrected for instrumental resolution. The temperature shown in this paper was corrected for laser heating [28].

Group theory analysis. Group theory predictions were performed using the tool provided in the ISOTROPY software suite and the Bilbao Crystallographic Server [34–36]. The information for the irreducible representations of point groups and space groups follows the notation of Cracknell *et al.* [37], which is the same for the Bilbao Crystallographic Server [35,38].

III. RESULTS AND DISCUSSION

A. Phonon modes

The high-temperature phase of Mo_3Al_2C ($T > T^*$) belongs to a cubic structure with space group $P4_132$ or $P4_332$ [point group O (432)] at room temperature [Fig. 1(a)]. One of the phases ($P4_132$ or $P4_332$) is dominant in the sample we studied [28]. The Mo, Al, and C atoms have Wyckoff positions of 12d, 8c, and 4b, respectively. From the group theoretical considerations, Γ point phonon modes of cubic Mo_3Al_2C can be expressed as $\Gamma_{tot} = 2A_1 + 4A_2 + 6E + 8T_2 + 10T_1$. Raman active modes $\Gamma_{Raman} = 2A_1 + 6E + 8T_2$, and IR active modes are $\Gamma_{IR} = 9T_1$. Note that T_1 signals might become Raman active under resonant conditions [39]. The acoustic mode is $\Gamma_{acoustic} = T_1$. Here, we use the notation in the high-temperature phase for the discussion of the phonon modes and their temperature dependence.

For the O point group, the Raman selection rules indicate that the XX, XY, $X'X'$, $X'Y'$, RR, and RL polarization geometries probe the $A_1 + 4E$, $T_1 + T_2$, $A_1 + E + T_2$, $3E + T_1$, $A_1 + E + T_1$, and $3E + T_2$ symmetry excitations, respectively. Symmetry analysis for point group O is summarized in Table I [33]. The algebra used to decompose measured Raman spectra into four irreducible representations for point group O are shown in Table II [33].

In Fig. 2(a), we show the phonon spectra of Mo_3Al_2C at room temperature in the six measured scattering geometries for a polished (0 0 1) surface. Several phonon modes with A_1, E, and T_2 symmetries are observed in these scattering geometries. As we show the symmetry decompositions according to point group O (Table II) in Fig. 2(b), these phonon modes are separated into the A_1, E, T_1, and T_2 symmetry channels. In the A_1 symmetry channel, we detect two phonon modes at 180 and 319 cm^{-1}, corresponding to Mo and Al fully symmetric lattice vibrations, respectively. In the T_2 symmetry channel, we detect three phonons at 129, 190, and 415 cm^{-1}. Note that the low-energy T_2 at 129 cm^{-1} leaks into the A_1 symmetry channel, creating a weak peak in the A_1 symmetry channel. This leakage signal might be due to imperfect cutting and

TABLE I. The relationship between the scattering geometries from a (0 0 1) surface and the symmetry channels for the high-temperature phase. A_1, E, T_1, and T_2 are the irreducible representations of the O point group. X, Y, X', and Y' represent the [1 0 0], [0 1 0], [1 1 0], [1 −1 0] directions. R and L represent the right and left circular polarizations defined on the (0 0 1) surface, respectively.

Scattering geometry	Symmetry channel (O)
XX	$A_1 + 4E$
XY	$T_1 + T_2$
$X'X'$	$A_1 + E + T_2$
$X'Y'$	$3E + T_1$
RR	$A_1 + E + T_1$
RL	$3E + T_2$

TABLE II. The algebra used in this study to decompose the Raman data from the (0 0 1) surface into four irreducible representations of point group O.

Symmetry channel	Expression
A_1	$(1/3)(XX + X'X' + RR - X'Y' - RL)$
E	$(1/6)(X'Y' + RL - XY)$
T_1	$(1/2)(XY + RR - X'X')$
T_2	$(1/2)(XY + RL - X'Y')$

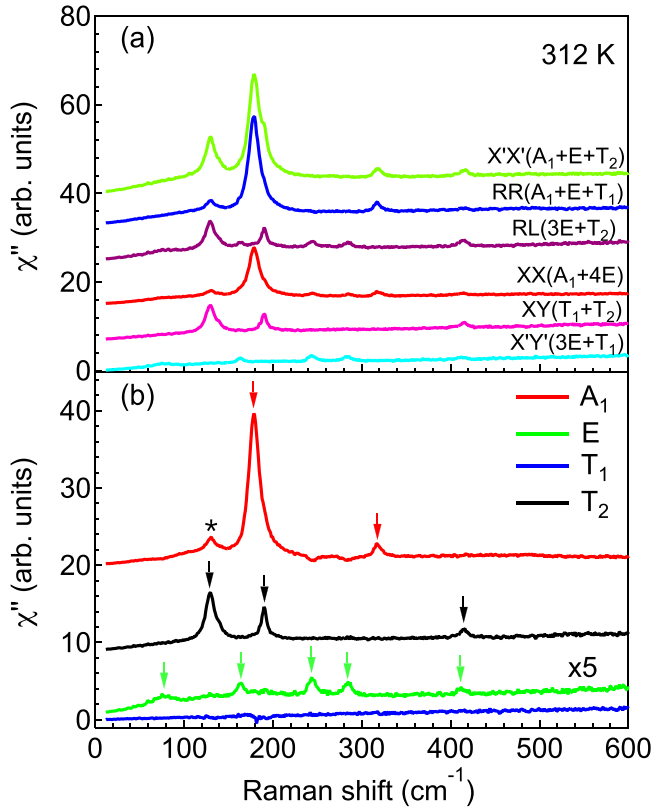

FIG. 2. (a) Raman spectra of Mo_3Al_2C from a polished (0 0 1) surface for the XX, XY, $X'X'$, $X'Y'$, RR, and RL scattering geometries at 312 K. (b) Symmetry decompositions into separate irreducible representations according to the point group O using the algebra shown in Table II. The star in (b) represents the leakage phonon intensity from the T_2 phonon at 129 cm^{-1}.

polishing of the single crystal. In the E symmetry channel, we observe five phonon modes at 75, 164, 245, 285, and 413 cm^{-1}. These E symmetry phonon intensities are generally 5 times weaker than the T_2 symmetry phonons. The four sharp E modes are first-order phonons, while the broad one at 75 cm^{-1} is a second-order two-phonon excitation because the linewidth is 4 times that of the three sharp ones. In the T_1 antisymmetric channel, we barely detect any phonon modes. The peak positions of the A_1, E, and T_2 phonons are summarized in Table IV.

Upon cooling below $T^* = 155$ K, Mo_3Al_2C undergoes a CDW transition and becomes a rhombohedral $R3$ structure with point group C_3. The primitive cell at low temperature becomes a $2 \times 2 \times 1$ superstructure and thus 4 times larger in the hexagonal setting [28]. The correlation table for point group O indicates that the A_1 and A_2 irreducible representations merge into the A irreducible representation in the $R3$ phase, the E irreducible representation does not change, and the T_2 irreducible representation splits into $A + E$ in the $R3$ phase [28]. From the group theoretical considerations, the Γ point phonon modes of the rhombohedral Mo_3Al_2C can be expressed as $\Gamma_{tot} = 96A \oplus 96E$. Raman active modes and IR active modes are $\Gamma_{Raman} = \Gamma_{IR} = 95A \oplus 95E$, and the acoustic mode $\Gamma_{acoustic} = A \oplus E$. Note that the fully symmetric carbon lattice vibration mode becomes Raman active in the C_3 phase below T^*.

TABLE III. The relationship between the scattering geometries from a (1 1 1) surface and the symmetry channels for the high-temperature phase. A_1, E, T_1, and T_2 are the irreducible representations of the O point group. The selection rules on the (1 1 1) surface are independent of the in-plane angle rotations. Examples of the X and Y directions are the [1 −10] and [11 −2] directions. R and L represent the right and left circular polarizations defined on the (1 1 1) surface, respectively.

Scattering geometry	Symmetry channel (O)
XX	$A_1 + E + T_2$
XY	$E + T_1 + \frac{2}{3}T_2$
RR	$A_1 + T_1 + \frac{1}{3}T_2$
RL	$2E + \frac{4}{3}T_2$

As shown in Figs. 3(a), 3(c) and 3(e), several low-energy A symmetry modes appear below 100 cm^{-1} in the parallel scattering geometries below T^*. They correspond to the Mo lattice vibration modes according to the DFT phonon calculation [40]. Specifically, the broad peak at around 50 cm^{-1} appearing at low temperatures is the amplitude mode of the CDW order parameter [28]. Furthermore, a noticeable A symmetry peak at around 500 cm^{-1} appears in the XX, $X'X'$, and RR scattering geometries below T^*. A weaker E symmetry peak at around 520 cm^{-1} appears in the $X'Y'$ and RL scattering geometries. These modes correspond to the carbon lattice vibrations modes [40], which appear only in the symmetry-broken state according to group theoretical analysis. Last, below T^*, the four first-order E symmetry phonon modes do not split because they can be fitted by a single Lorentzian function, as shown in Figs. 5(e)–5(h). In the XY scattering geometry, we detect two T_2 symmetry phonons at 129 and 190 cm^{-1} at 312 K. They split into two modes in the 26 K data, as shown in Figs. 5(i)–5(l).

In Fig. 4, we present the Raman response of Mo_3Al_2C at 312 and 66 K in the four measured scattering geometries from a polished (1 1 1) surface. The phonon spectra at 312 and 66 K are consistent with the Raman data measured from the (0 0 1) surface (Figs. 2 and 3). Regarding the selection rule for the (1 1 1) surface (Table III) [33], the A_1 and E

TABLE IV. Summary of experimental phonon mode symmetries and frequencies for Mo_3Al_2C at 312 K.

Symmetry	Expt. (cm^{-1})
E	75
T_2	129
E	164
A_1	180
T_2	190
E	245
E	285
A_1	319
E	413
T_2	415

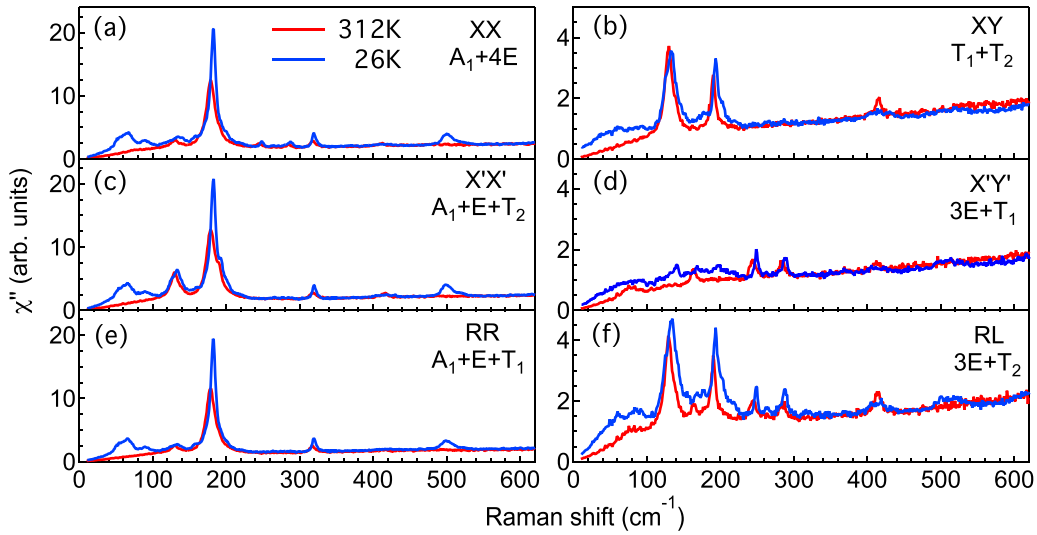

FIG. 3. Raman spectra of Mo_3Al_2C on a polished (0 0 1) surface for the (a) XX, (b) XY, (c) $X'X'$, (d) $X'Y'$, RR (e), and (f) RL scattering geometries at 312 and 26 K.

irreducible representations can be separated in the RR and RL scattering geometries, respectively. This is impossible for the Raman response from the (0 0 1) surface because the phonons with A_1 and E symmetries always appear together in the parallel scattering geometries. This point is rather helpful in the discussion of the second-order Raman response in the next section.

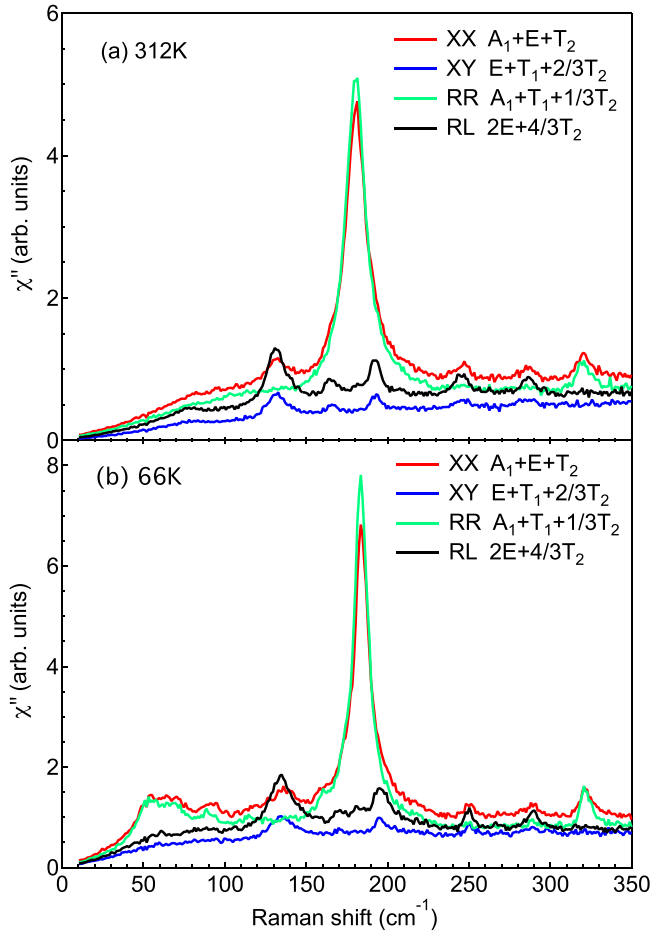

FIG. 4. Raman spectra of Mo_3Al_2C from a polished (1 1 1) surface for the XX, XY, RR, and RL scattering geometries at (a) 312 K and (b) 66 K.

B. Temperature dependence

After establishing the phonon modes in Mo_3Al_2C, we switch to studying their temperature dependence.

In Fig. 5, we show the fitting results for data in the XX, $X'Y'$, and XY scattering geometries from the (0 0 1) surface of Mo_3Al_2C at selected temperatures (312, 151, 91, and 26 K) using multi-Lorentzian peaks fitted on a smooth background [33]. In Fig. 6, we present the temperature dependence of the peak frequencies, half width at half maximum (HWHM), and intergraded area for these A_1, E, and T_2 phonon modes.

As shown in Fig. 6(a), the A_1 phonon mode at 180 cm^{-1} hardens upon cooling. It shows substantial additional hardening upon cooling below T^*, suggesting this mode couples to the CDW order parameter. Below $T' \sim 100$ K, the A_1 phonon mode at 180 cm^{-1} shows a saturationlike behavior. The anomaly at T' is also found in the T dependence of the resistivity curve where the slope changes sign at T'; namely, $d\rho/dT$ is zero at around T' [Fig. 1(b)]. The temperature dependence of the mode frequency follows well the anharmonic phonon decay model (Appendix A) in both temperature ranges $T > T^*$ and $T' < T < T^*$. On the contrary, the A_1 mode at 319 cm^{-1} decreases a little bit upon cooling below T^*, then increases, finally decreases again, and forms a local maximum at T'. For the HWHMs of these two modes, both of them decease upon cooling, showing anomalies at T^*. For the integrated area, the A_1 phonon mode at 180 cm^{-1} shows an increase upon cooling and decreases below T^*. In contrast, the A_1 phonon mode at 319 cm^{-1} increases continuously upon cooling, indicating the finite electron-phonon coupling in this system [41]. We note that the E mode at 140 cm^{-1} in the $X'Y'$ scattering geometry [Figs. 3(d), 5(e), and 5(f)], which appears only below T^*, shows the Fano line shape reported in previous studies [42,43]. The asymmetric line shape for this

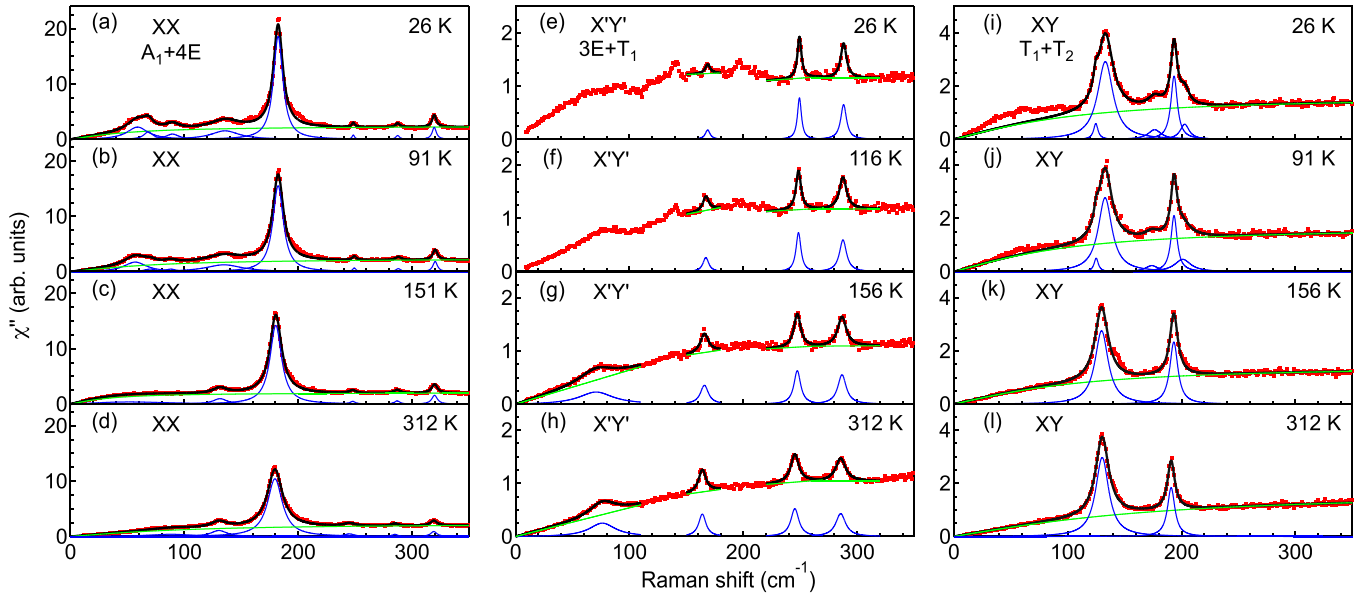

FIG. 5. Selected fitting results in the XX, $X'Y'$, and XY scattering geometries on the (0 0 1) plane of Mo_3Al_2C at 312, 151, 91, and 26 K using Lorentzian function fitting on a smooth background. (a)–(d) are for the XX scattering geometry, (e)–(h) are for the $X'Y'$ scattering geometry, and (i)–(l) are for the XY scattering geometry. The black solid curves denote the total response. The green curves denote the backgrounds. The blue curves denote the individual components.

mode also supports the existence of electron-phonon coupling in this system.

For the E modes at 164, 245, and 285 cm^{-1}, these three phonons harden upon cooling, showing additional hardening below T^*. The additional hardening is larger for the mode at 164 cm^{-1} than the other two modes [Figs. 6(j), 6(m) and 6(p)]. These three phonon modes narrow upon cooling. The HWHMs for the modes at 164 and 285 cm^{-1} follow well the anharmonic phonon decay model [Figs. 6(k) and 6(q)], while the mode at 245 cm^{-1} narrows much faster below T^* [Fig. 6(n)]. For the integrated area, the two phonons at 245 and 285 cm^{-1} remain almost constant [Figs. 6(o) and 6(r)], while the integrated area decreases quickly for the mode at 164 cm^{-1} below T^* [Fig. 6(l)].

The E mode at 75 cm^{-1} softens to 70 cm^{-1} from 312 K to T^* [Fig. 6(g)]. In contrast, the linewidth and the integrated area for this mode increase slightly upon cooling close to T^* [Figs. 6(h) and 6(i)]. Note that the linewidth of the 75 cm^{-1} mode is 4 times those of the other E modes. The softening of the 75 cm^{-1} mode above T^*, the spectrum line shape change below T^*, and its large linewidth broadening suggest that it is not a regular first-order phonon mode, but rather a second-order phonon that reflects the softening phonon branch around M points [28], similar to what was found in the study of 2H-$NbSe_2$ [44]. The softening of the phonon branch at the M point could be probed by future momentum-resolved spectroscopies, such as electron energy loss spectroscopy or inelastic neutron/x-ray scattering spectroscopy. This E-type

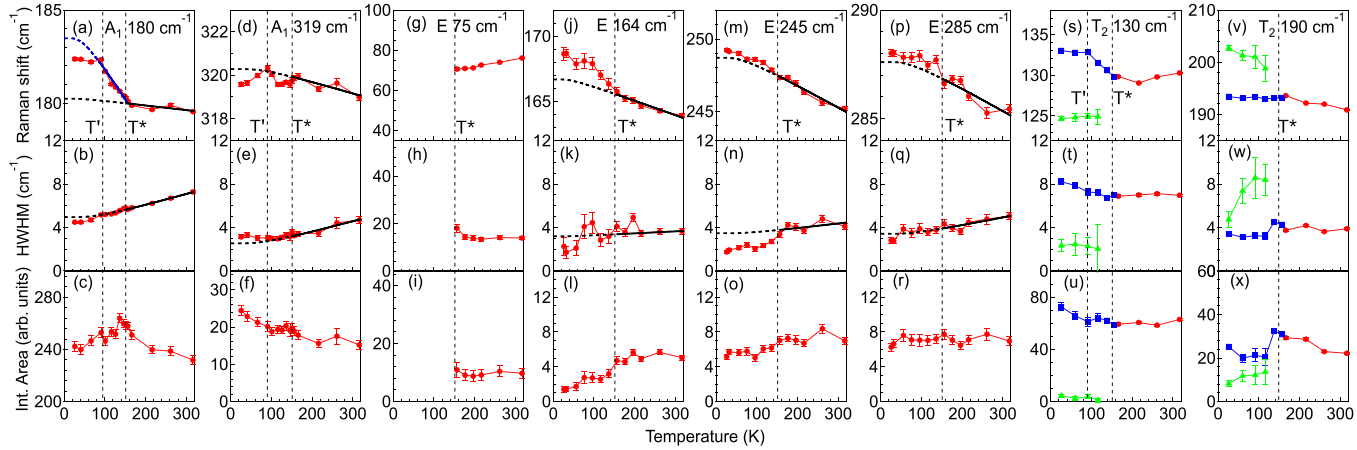

FIG. 6. T dependence of the fitting parameters [peak frequency, half width at half maximum (HWHM), integrated area] for the A_1, E, and T_2 phonon modes. (a)–(c) are for the A_1 mode at 180 cm^{-1}, (d)–(f) are for the A_1 mode at 319 cm^{-1}, (g)–(i) are for the E mode at 75 cm^{-1}, (j)–(l) are for the E mode at 164 cm^{-1}, (m)–(o) are for the E mode at 245 cm^{-1}, (p)–(r) are for the E mode at 285 cm^{-1}, (s)–(u) are for the T_2 mode at 130 cm^{-1}, and (v)–(x) are for the T_2 mode at 190 cm^{-1}. The dashed vertical lines represent T^* at 155 K and T' at around 100 K.

second-order phonon is symmetry allowed based on the direct product rules: $M_5 \otimes M_5 = \Gamma_1(A_1) \oplus \Gamma_3(E) \oplus \Gamma_4(T_1) \oplus \Gamma_5(T_2)$ (Appendix B). The details of the second-order scattering process are given in Appendix B. Generally, for second-order Raman scattering, the identity representation $\Gamma_1(A_1)$ produces scattering efficiencies considerably stronger than those of the other channels, as is the case for Si [45]. For Mo_3Al_2C, the second-order Raman scattering intensity is more noticeable in the E symmetry channel [RL in Fig. 4(a)] than that in the A_1 symmetry channel [RR in Fig. 4(a)], rendering Mo_3Al_2C a special case for second-order Raman scattering.

For the T_2 phonon modes, these two modes at 130 and 190 cm^{-1} are observed above T^*, as shown in Figs. 5(i)–5(l). Below T^*, the T_2 mode splits into two modes, as shoulder peaks can be seen on the left side of the mode at 130 cm^{-1} and on the right side of the mode at 190 cm^{-1}. The splitting of the T_2 phonon modes is due to the symmetry breaking as a result of the CDW order below T^* [28]. The splittings can be seen from the fitting of these modes shown in Figs. 5(i)–5(l). Above T^*, a single Lorentzian function can describe the T_2 phonon well, while it requires two Lorentzian functions to model the T_2 phonon below T^*. Note that a separate peak at 177 cm^{-1} appears below T^*. It is a new mode, and it does not belong to one of the components of the T_2 mode at 190 cm^{-1}.

The fitting parameters for the T_2 phonon modes are presented in Figs. 6(s)–6(x). For the T_2 mode at 130 cm^{-1}, it softens 1 cm^{-1} upon cooling from 312 to 200 K [Fig. 6(s)], while the HWHM and the integrated area barely change [Figs. 6(t) and 6(u)]. Below T^*, it splits into two modes: One is at 125 cm^{-1}, and the other one is at 133 cm^{-1}. For the T_2 mode at 190 cm^{-1}, it hardens slightly upon cooling [Fig. 6(v)], while the HWHM barely changes [Fig. 6(w)] and the integrated area increases slightly [Fig. 6(x)]. Below T^*, it splits into two modes: One is at 193 cm^{-1}, and the other one is at 202 cm^{-1}. We note that the high-energy component of the split 130 cm^{-1} mode shows an anomaly at T'; namely, the T dependence of the mode's frequency shows a saturationlike behavior below T' [Fig. 6(s)], similar to the A_1 mode at 180 cm^{-1} [Fig. 6(a)].

Finally, we discuss the origin of the phonon and resistivity anomalies at T'. Based on the density functional theory phonon calculations, there are three unstable phonon modes in the phonon dispersion for the cubic phase of Mo_3Al_2C: Γ_4 (0, 0, 0), M_5 (0.5, 0.5, 0), and X_2 (0.5, 0.5, 0) [28,40]. In our previous study [28], we showed that Mo_3Al_2C undergoes a cubic-nonpolar to rhombohedral-polar transition below T^* into an $R3$ phase, which is driven by condensation of the M_5 soft modes at three symmetry-equivalent wave vectors located at the Brillouin zone boundary, and creates a polarization along the threefold axis in the body-diagonal direction below T^*. The analysis of the T dependence of the superlattice Bragg peaks and polar domain imaging support that the CDW transition and the polar transition occur at the same temperature T^* [33]. From the T dependence of the Raman response in the XX, XY, and $X'Y'$ scattering geometries (Fig. 5 here and Fig. 3 in Ref. [28]), the number of new phonon modes does not change below T'; thus, the phonon anomalies at T' do not seem to be related to zone-boundary lattice instabilities. Furthermore, the twofold-degenerate E modes at 245 and 285 cm^{-1} do not show signatures of splitting within our energy resolution (1.5 cm^{-1} based on the full width at half maximum for the laser line) in the $R3$ phase (Figs. 3 and 5). The linewidths for these E modes do not show noticeable broadening upon cooling across T' [Figs. 6(n) and 6(q)].

The deviation from the anharmonic behavior of the A_1 mode at 180 cm^{-1} below T' could be due to either lattice distortion, electron-phonon coupling, or spin-phonon coupling. The A_1 mode at 180 cm^{-1} shows a symmetric line shape between 300 and 26 K and can be modeled by a Lorentzian line shape (Fig. 5). Thus, the electron-phonon coupling mechanism is not likely. The absence of magnetic order in Mo_3Al_2C from the magnetic susceptibility measurement [30] suggests that spin-phonon coupling could not account for the phonon anomaly at T'.

One possible explanation for the phonon anomalies at T' could be a fully symmetric modification of the Mo lattice structure while the overall C_3 point group symmetry is preserved because the Mo lattice related vibration modes [40], especially for the T_2 mode at 130 cm^{-1} and the A_1 mode at 180 cm^{-1}, show clear saturationlike behaviors below T'. The fully symmetric modification of the crystal structure in Mo_3Al_2C below T' might resemble the case in $Na_{0.5}CoO_2$, where the overall space group symmetry for $Na_{0.5}CoO_2$ remains $Pnmm$ between 300 and 10 K [46,47] but the Na-O bond lengths show multiple anomalies in the same temperature range according to the neutron powder diffraction structural refinements [48]. We note that the temperature dependence of the amplitude mode at around 50 cm^{-1} in the CDW phase (Figs. 3(f)–3(h) of Ref. [28]) shows a smooth evolution upon cooling across T'. This suggests that the fully symmetric modification of the Mo lattice structure below T' is secondary to the dominant lattice distortion due to the soft mode, which condenses below the CDW transition. This point is also supported by the temperature dependence of the resistivity curve, where a gradual change in the resistivity slope is found at T', in contrast to the clear dip found at T^* [Fig. 1(b)]. Thus, the physics for triggering the change in the modulation pattern associated with the Mo lattice across T' is different from what is dictated by the M_5 soft mode eigenvectors.

While we cannot completely rule out a symmetry-breaking phase transition at T' based on our current energy resolution in the Raman experiment, future high-resolution x-ray structure refinement investigations of the lattice structure below T^* and T' could determine the details of the phase transitions and lattice anomalies in Mo_3Al_2C.

IV. CONCLUSIONS

In summary, we studied the lattice dynamics of the polar CDW phase of the superconductor Mo_3Al_2C using polarization-resolved Raman spectroscopy. We investigated the temperature dependence of the phonon modes' frequency, half width at half maximum, and integrated area below $T^* = 155$ K and found anomalies at an intermediate temperature, $T' \sim 100$ K, for the modes at 130 and 180 cm^{-1}. We inferred that the lattice anomalies at T' are possibly related to a fully symmetric modification of Mo displacements within the CDW phase while the lattice symmetry is preserved; high-resolution x-ray structure refinement investigations of the lattice

distortions below T^* and T' are required to further understand the phase transitions and lattice anomalies in the polar CDW compound Mo_3Al_2C. Our results in this paper provide detailed lattice dynamics information for Mo_3Al_2C, forming a basis for future studies of the superconducting state in Mo_3Al_2C which processes both structural polarity and chirality, e.g., switchable ferroelectric superconductivity [49], nonreciprocal charge transport [50,51], and the unconventional pairing mechanism [52,53].

ACKNOWLEDGMENTS

The spectroscopy work at Rutgers (S.W. and G.B.) was supported by NSF Grant No. DMR-2105001. The work at BAQIS (S.W.) was supported by the National Natural Science Foundation of China (Grant No. 12404548). The sample growth, characterization, and TEM work (X.X., F.-T.H, and S.-W.C.) was supported by a W. M. Keck Foundation grant to the Keck Center for Quantum Magnetism at Rutgers University. T.B. was supported by the Department of Energy through the University of Minnesota Center for Quantum Materials under Grant No. DESC0016371. The work at NICPB was supported by the European Research Council (ERC) under the European Union's Horizon 2020 research and innovation program, Grant Agreement No. 885413.

DATA AVAILABILITY

The data that support the findings of this article are not publicly available upon publication because it is not technically feasible and/or the cost of preparing, depositing, and hosting the data would be prohibitive within the terms of this research project. The data are available from the authors upon reasonable request.

APPENDIX A: ANHARMONIC PHONON DECAY MODEL

In this Appendix, we discuss the anharmonic phonon decay model. We fit the temperature dependence of the phonon frequency and HWHM using the anharmonic phonon decay model [54,55]:

$$\omega_1(T) = \omega_0 - C_1\{1 + 2n[\Omega(T)/2]\}, \tag{A1}$$

$$\Gamma_1(T) = \gamma_0 + \gamma_1\{1 + 2n[\Omega(T)/2]\}, \tag{A2}$$

where $\Omega(T) = \hbar\omega/k_BT$ and $n(x) = 1/(e^x - 1)$ is the Bose-Einstein distribution function. $\omega_1(T)$ and $\Gamma_1(T)$ involve mainly the three-phonon decay process, in which an optical phonon decays into two acoustic modes with equal energies and opposite momenta.

APPENDIX B: DIRECT PRODUCT OF $M_5 \otimes M_5$

In this Appendix, we study the possibility of two-phonon Raman processes due to the M_5 modes. The combination of two M_5 phonons with the same wave vector can couple with a number of modes from the Γ point, whereas the combination of two M_5 phonons from different M points can couple with phonons from the only other M point in the Brillouin zone. The complete list of modes that two M_5 modes couple to can be predicted by taking the product M_5 irreducible representation (irrep) by itself, i.e., $M_5 \otimes M_5$, and decomposing it into irreducible representations of the space group. Since M_5 is a six-dimensional irrep (it has a two-dimensional little group irrep on each of the three different M points in the star), this product is 36-dimensional. Only 9 of these 36 degrees of freedom are at the Γ point, and they are

$$M_5 \otimes M_5 = \Gamma_1 \oplus \Gamma_3 \oplus \Gamma_4 \oplus \Gamma_5 + (\cdots), \tag{B1}$$

where $(\cdots)$ includes irreps from the M point. In other words, the two-phonon processes from M_5 modes can couple with a Γ_1, Γ_3, Γ_4, or Γ_5 phonon. (Using the point group irrep labels, these are the A_1, E, T_1, and T_2 modes, respectively.)

The next question that is relevant is what combinations of the 6 degrees of freedom of the M_5 modes couple with these modes. In the following, for simplicity, we denote the six symmetry adapted components of $M_5(a, b; c, d; e, f)$ as $(M_{1a}, M_{1b}, M_{2a}, M_{2b}, M_{3a}, M_{3b})$, respectively. If we denote the only component of the fully symmetric irrep Γ_1 as Γ_1, the coupling term that is second order in M_5 and first order in Γ_1 (A_1) is

$$\Gamma_1\left(M_{1a}^2 + M_{1b}^2 + M_{2a}^2 + M_{2b}^2 + M_{3a}^2 + M_{3b}^2\right). \tag{B2}$$

Similarly, the coupling between Γ_3 (E), whose components we denote as Γ_{3a} and Γ_{3b}, is

$$\Gamma_{3a}\left(M_{1a}^2 + M_{1b}^2 - \frac{1}{2}\left[M_{2a}^2 + M_{2b}^2 + M_{3a}^2 + M_{3b}^2\right]\right) + \frac{\sqrt{3}}{2}\Gamma_{3b}\left(M_{2a}^2 + M_{2b}^2 - M_{3a}^2 - M_{3b}^2\right). \tag{B3}$$

With a similar notation, the coupling to Γ_4 (T_1) is

$$\Gamma_{4a}M_{1a}M_{1b} + \Gamma_{4b}M_{2a}M_{2b} + \Gamma_{4c}M_{3a}M_{3b}, \tag{B4}$$

and the coupling to Γ_5 (T_2) is

$$\Gamma_{5a}\left(M_{1a}^2 - M_{1b}^2\right) + \Gamma_{5b}\left(M_{2a}^2 - M_{2b}^2\right) + \Gamma_{5c}\left(M_{3a}^2 - M_{3b}^2\right). \tag{B5}$$

[1] P. W. Anderson and E. I. Blount, Symmetry considerations on martensitic transformations: "Ferroelectric" metals? Phys. Rev. Lett. **14**, 217 (1965).
[2] N. A. Benedek and T. Birol, 'Ferroelectric' metals reexamined: Fundamental mechanisms and design considerations for new materials, J. Mater. Chem. C **4**, 4000 (2016).
[3] D. Hickox-Young, D. Puggioni, and J. M. Rondinelli, Polar metals taxonomy for materials classification and discovery, Phys. Rev. Mater. **7**, 010301 (2023).
[4] W. X. Zhou and A. Ariando, Review on ferroelectric/polar metals, Jpn. J. Appl. Phys. **59**, SI0802 (2020).
[5] P. Ghosez and J. Junquera, Modeling of ferroelectric oxide perovskites: From first to second principles, Annu. Rev. Condens. Matter Phys. **13**, 325 (2022).
[6] S. Bhowal and N. A. Spaldin, Polar metals: Principles and prospects, Annu. Rev. Mater. Res. **53**, 53 (2023).
[7] D. Puggioni and J. M. Rondinelli, Designing a robustly metallic noncenstrosymmetric ruthenate oxide with

large thermopower anisotropy, Nat. Commun. **5**, 3432 (2014).

[8] T. H. Kim, D. Puggioni, Y. Yuan, L. Xie, H. Zhou, N. Campbell, P. J. Ryan, Y. Choi, J.-W. Kim, J. R. Patzner, S. Ryu, J. P. Podkaminer, J. Irwin, Y. Ma, C. J. Fennie, M. S. Rzchowski, X. Q. Pan, V. Gopalan, J. M. Rondinelli, and C. B. Eom, Polar metals by geometric design, Nature (London) **533**, 68 (2016).

[9] X. He and K.-J. Jin, Persistence of polar distortion with electron doping in lone-pair driven ferroelectrics, Phys. Rev. B **94**, 224107 (2016).

[10] Y. Shi, Y. Guo, X. Wang, A. J. Princep, D. Khalyavin, P. Manuel, Y. Michiue, A. Sato, K. Tsuda, S. Yu, M. Arai, Y. Shirako, M. Akaogi, N. Wang, K. Yamaura, and A. T. Boothroyd, A ferroelectric-like structural transition in a metal, Nat. Mater. **12**, 1024 (2013).

[11] S. Lei, M. Gu, D. Puggioni, G. Stone, J. Peng, J. Ge, Y. Wang, B. Wang, Y. Yuan, K. Wang, Z. Mao, J. M. Rondinelli, and V. Gopalan, Observation of quasi-two-dimensional polar domains and ferroelastic switching in a metal, $Ca_3Ru_2O_7$, Nano Lett. **18**, 3088 (2018).

[12] N. A. Benedek and C. J. Fennie, Hybrid improper ferroelectricity: A mechanism for controllable polarization-magnetization coupling, Phys. Rev. Lett. **106**, 107204 (2011).

[13] Z. Fei, W. Zhao, T. A. Palomaki, B. Sun, M. K. Miller, Z. Zhao, J. Yan, X. Xu, and D. H. Cobden, Ferroelectric switching of a two-dimensional metal, Nature (London) **560**, 336 (2018).

[14] H. Sakai, K. Ikeura, M. S. Bahramy, N. Ogawa, D. Hashizume, J. Fujioka, Y. Tokura, and S. Ishiwata, Critical enhancement of thermopower in a chemically tuned polar semimetal $MoTe_2$, Sci. Adv. **2**, e1601378 (2016).

[15] K. F. Garrity, K. M. Rabe, and D. Vanderbilt, Hyperferroelectrics: Proper ferroelectrics with persistent polarization, Phys. Rev. Lett. **112**, 127601 (2014).

[16] S.-W. Cheong and M. Mostovoy, Multiferroics: A magnetic twist for ferroelectricity, Nat. Mater. **6**, 13 (2007).

[17] J. van den Brink and D. I. Khomskii, Multiferroicity due to charge ordering, J. Phys.: Condens. Matter **20**, 434217 (2008).

[18] M. Fiebig, T. Lottermoser, D. Meier, and M. Trassin, The evolution of multiferroics, Nat. Rev. Mater. **1**, 16046 (2016).

[19] M. Alexe, M. Ziese, D. Hesse, P. Esquinazi, K. Yamauchi, T. Fukushima, S. Picozzi, and U. Gösele, Ferroelectric switching in multiferroic magnetite Fe_3O_4 thin films, Adv. Mater. **21**, 4452 (2009).

[20] D. V. Efremov, J. van den Brink, and D. I. Khomskii, Bond-versus site-centred ordering and possible ferroelectricity in manganites, Nat. Mater. **3**, 853 (2004).

[21] J. A. Alonso, J. L. García-Muñoz, M. T. Fernández-Díaz, M. A. G. Aranda, M. J. Martínez-Lope, and M. T. Casais, Charge disproportionation in $RNiO_3$ perovskites: Simultaneous metal-insulator and structural transition in $YNiO_3$, Phys. Rev. Lett. **82**, 3871 (1999).

[22] N. Ikeda, H. Ohsumi, K. Ohwada, K. Ishii, T. Inami, K. Kakurai, Y. Murakami, K. Yoshii, S. Mori, Y. Horibe, and H. Kitô, Ferroelectricity from iron valence ordering in the charge-frustrated system $LuFe_2O_4$, Nature (London) **436**, 1136 (2005).

[23] J. de Groot, T. Mueller, R. A. Rosenberg, D. J. Keavney, Z. Islam, J.-W. Kim, and M. Angst, Charge order in $LuFe_2O_4$: An unlikely route to ferroelectricity, Phys. Rev. Lett. **108**, 187601 (2012).

[24] S. Y. Park, A. Kumar, and K. M. Rabe, Charge-order-induced ferroelectricity in $LaVO_3/SrVO_3$ superlattices, Phys. Rev. Lett. **118**, 087602 (2017).

[25] A. L. Krick, C.-W. Lee, R. J. Sichel-Tissot, A. M. Rappe, and S. J. May, Interplay between cation and charge ordering in $La_{1/3}Sr_{2/3}FeO_3$ superlattices, Adv. Electron. Mater. **2**, 1500372 (2016).

[26] Y. Qi and K. M. Rabe, Electron-lattice coupling effects in nonadiabatic polarization switching of charge-order-induced ferroelectrics, Phys. Rev. B **106**, 125131 (2022).

[27] S. Xu, X. Xu, and S. Xu, Charge-gradient-induced ferroelectricity with robust polarization reversal, Nano Lett. **23**, 298 (2023).

[28] S. Wu, F.-T. Huang, X. Xu, E. Ritz, T. Birol, S.-W. Cheong, and G. Blumberg, Polar charge density wave in a superconductor with crystallographic chirality, Nat. Commun. **15**, 9276 (2024).

[29] N. D. Zhigadlo, D. Logvinovich, V. A. Stepanov, R. S. Gonnelli, and D. Daghero, Crystal growth, characterization, and point-contact Andreev-reflection spectroscopy of the noncentrosymmetric superconductor Mo_3Al_2C, Phys. Rev. B **97**, 214518 (2018).

[30] T. Koyama, Y. Maeda, T. Yamazaki, K.-I. Ueda, T. Mito, T. Kohara, T. Waki, Y. Tabata, H. Tsunemi, M. Ito, and H. Nakamura, Normal and superconducting properties of the noncentrosymmetric Mo_3Al_2C, J. Phys. Soc. Jpn. **82**, 073709 (2013).

[31] T. Koyama, Y. Ozaki, K. Ueda, T. Mito, T. Kohara, T. Waki, Y. Tabata, C. Michioka, K. Yoshimura, M.-T. Suzuki, and H. Nakamura, Partial gap opening on the Fermi surface of the noncentrosymmetric superconductor Mo_3Al_2C, Phys. Rev. B **84**, 212501 (2011).

[32] C. N. Kuo, H. F. Liu, and C. S. Lue, NMR characteristics in noncentrosymmetric Mo_3Al_2C, Phys. Rev. B **85**, 052501 (2012).

[33] See Supplemental Material at http://link.aps.org/supplemental/10.1103/nkx2-6qyr for a comparison between the as-grown and polished samples, the Raman tensor analysis, the details of the multi-Lorentzian fitting, and an analysis of the T dependence of the TEM diffraction patterns and the polar domain imaging, which includes Refs. [28,56,57].

[34] E. Kroumova, M. I. Aroyo, J. M. Perez-Mato, A. Kirov, C. Capillas, S. Ivantchev, and H. Wondratschek, Bilbao crystallographic server: Useful databases and tools for phase-transition studies, Ph. Transit. **76**, 155 (2003).

[35] M. I. Aroyo, J. M. Perez-Mato, D. Orobengoa, E. Tasci, G. De La Flor, and A. Kirov, Crystallography online: Bilbao crystallographic server, Bulg. Chem. Commun. **43**, 183 (2011).

[36] D. M. Hatch and H. T. Stokes, Invariants: Program for obtaining a list of invariant polynomials of the order-parameter components associated with irreducible representations of a space group, J. Appl. Crystallogr. **36**, 951 (2003).

[37] A. P. Cracknell, B. L. Davies, S. C. Miller, and W. F. Love, *Kronecker Product Tables,* General Introduction and Tables of Irreducible Representations of Space Groups (IFI/Plenum, New York, 1979), Vol. 1.

[38] M. I. Aroyo, A. Kirov, C. Capillas, J. M. Perez-Mato, and H. Wondratschek, Bilbao crystallographic server. II. Representations of crystallographic point groups and space groups, Acta Crystallogr. Sect. A **62**, 115 (2006).

[39] G. Placzek, The Rayleigh and Raman Scattering, in *Handbuch der Radiologie*, edited by E. Marx, (Leipzig, Akademische Verlagsgesellschaft, 1934), VI, 2, pp. 209–374.

[40] D. Reith, C. Blaas-Schenner, and R. Podloucky, Density functional theory study of phase stability, vibrational, and electronic properties of Mo_3Al_2C, Phys. Rev. B **86**, 104105 (2012).

[41] M. Ye, E. W. Rosenberg, I. R. Fisher, and G. Blumberg, Lattice dynamics, crystal-field excitations, and quadrupolar fluctuations of $YbRu_2Ge_2$, Phys. Rev. B **99**, 235104 (2019).

[42] B. Xu, Y. M. Dai, L. X. Zhao, K. Wang, R. Yang, W. Zhang, J. Y. Liu, H. Xiao, G. F. Chen, S. A. Trugman, J.-X. Zhu, A. J. Taylor, D. A. Yarotski, R. P. Prasankumar, and X. G. Qiu, Temperature-tunable Fano resonance induced by strong coupling between Weyl fermions and phonons in TaAs, Nat. Commun. **8**, 14933 (2017).

[43] S.-F. Wu, W.-L. Zhang, L. Li, H.-B. Cao, H.-H. Kung, A. S. Sefat, H. Ding, P. Richard, and G. Blumberg, Coupling of fully symmetric As phonon to magnetism in $Ba(Fe_{1-x}Au_x)_2As_2$, Phys. Rev. B **102**, 014501 (2020).

[44] A. Mialitsin, Raman scattering from layered superconductors: Effects of charge ordering, two-band superconductivity, and structural disorder, Ph.D. thesis, Rutgers University, 2010.

[45] M. Cardona, Resonance phenomena, in *Light Scattering in Solids II*, edited by M. Cardona and G. Güntherodt, Topics in Applied Physics (TAP, volume 50) (Springer-Verlag, Berlin, 1982), Chap. 2, p. 62.

[46] Q Huang, M. L. Foo, J. W Lynn, H. W. Zandbergen, G Lawes, Y. Wang, B. H. Toby, A. P. Ramirez, N. P. Ong, and R. J. Cava, Low temperature phase transitions and crystal structure of $Na_{0.5}CoO_2$, J. Phys.: Condens. Matter **16**, 5803 (2004).

[47] A. J. Williams, J. P. Attfield, M. L. Foo, L. Viciu, and R. J. Cava, High-resolution neutron diffraction study of possible charge ordering in $Na_{0.5}CoO_2$, Phys. Rev. B **73**, 134401 (2006).

[48] D. N. Argyriou, O. Prokhnenko, K. Kiefer, and C. J. Milne, Emergent charge ordering in near-half-doped $Na_{0.46}CoO_2$, Phys. Rev. B **76**, 134506 (2007).

[49] A. Jindal, A. Saha, Z. Li, T. Taniguchi, K. Watanabe, J. C. Hone, T. Birol, R. M. Fernandes, C. R. Dean, A. N. Pasupathy, and D. A. Rhodes, Coupled ferroelectricity and superconductivity in bilayer T_d-$MoTe_2$, Nature (London) **613**, 48 (2023).

[50] Y. Tokura and N. Nagaosa, Nonreciprocal responses from non-centrosymmetric quantum materials, Nat. Commun. **9**, 3740 (2018).

[51] M. Nadeem, M. S. Fuhrer, and X. Wang, The superconducting diode effect, Nat. Rev. Phys. **5**, 558 (2023).

[52] S. Yip, Noncentrosymmetric superconductors, Annu. Rev. Condens. Matter Phys. **5**, 15 (2014).

[53] C. Kallin and J. Berlinsky, Chiral superconductors, Rep. Prog. Phys. **79**, 054502 (2016).

[54] P. G. Klemens, Anharmonic decay of optical phonons, Phys. Rev. **148**, 845 (1966).

[55] J. Menéndez and M. Cardona, Temperature dependence of the first-order Raman scattering by phonons in Si, Ge, and $\alpha-$Sn: Anharmonic effects, Phys. Rev. B **29**, 2051 (1984).

[56] W. Hayes and R. Loudon, *Scattering of Light by Crystals* (Dover, New York, 1978).

[57] F.-T. Huang, S. J. Lim, S. Singh, J.-W. Kim, L. Zhang, J.-W. Kim, M.-W. Chu, K. M. Rabe, D. Vanderbilt, and S.-W. Cheong, Polar and phase domain walls with conducting interfacial states in a Weyl semimetal $MoTe_2$, Nat. Commun. **10**, 4211 (2019).